Uranus Orbiter and Probe: A Radio Science Investigation to Determine the Planet's Gravity Field, Depth of the Winds, and Tidal Deformations

Marzia Parisi [ORCID], A. James Friedson[1], Chris R. Mankovich, Mark D. Hofstadter [ORCID], Alex B. Akins [ORCID], Reza Karimi, and Damon F. Landau [ORCID]

Jet Propulsion Laboratory, California Institute of Technology, Pasadena, CA 91109, USA; marzia.parisi@jpl.nasa.gov

Abstract

The most recent Planetary Science and Astrobiology Decadal Survey has proposed Uranus as the target for NASA's next large-scale mission. The interior structure and atmosphere of the planet are currently poorly understood, and objectives for investigating Uranus's deeper regions and composition are highly ranked. Traditionally, gravity science has served as one of the primary means for probing the depths of planetary bodies and inferring their internal density distributions. In this work, we present precise numerical simulations of an onboard radio science experiment designed to determine Uranus's gravity field and tidal deformations, which would offer a rare view into the planet's interior. We focus on the mission's orbital planning, discussing crucial parameters such as the number of pericenter passes, orbital inclination, and periapsis altitude necessary to meet the gravity measurement requirements for a Uranus orbiter. Our findings suggest that eight close encounters may be sufficient to determine the zonal gravity field up to J_8 with a relative accuracy of 10%, if the trajectory is optimized. This would allow for the decoupling of the gravity field components due to interior structure and zonal winds. Additionally, we find that the expected end-of-mission uncertainty on Uranus's Love number k_{22} is of order ~ 0.01 (3σ). This level of accuracy may offer crucial information about Uranus's inner state and allow for discriminating between a liquid and solid core, thus shedding light on crucial aspects of the planet's formation and evolution.

Unified Astronomy Thesaurus concepts: Uranus (1751); Gravitational fields (667); Tides (1702); Orbiters (1183); Space probes (1545); Atmospheric dynamics (2300)

1. Introduction

An orbiter and probe to explore Uranus and its system have been recommended as NASA's highest-priority mission by the recent Planetary Science and Astrobiology Decadal Survey (National Academies of Sciences, Engineering, and Medicine 2022). This decision has fueled renewed interest in the unique characteristics of ice giant systems, which are generally still poorly understood. The planetary science community is currently engaging in collaborative efforts to identify the most effective investigations that align with the science questions outlined in the report, while concurrently taking notice of knowledge gaps that need further investigation. The envisioned science objectives for this mission concept are broad and encompass various fields, including the probing of the deep interior, dynamics and composition of the atmosphere, investigation of the magnetosphere, and a tour of the surrounding satellite and ring system. The path to achieving these goals must include a comprehensive and multidisciplinary approach. By tackling these critical areas, scientists aim to address pressing questions about the formation and evolution of the Uranian system, contributing to a deeper understanding of celestial bodies in our solar system and beyond.

Developing early plans for future science investigations is an essential step in planning space missions, and a key aspect is building on the experience gained from prior endeavors. When it comes to exploring planetary deep interiors, current methods available for such investigations are relatively limited. Traditionally, scientists have explored the internal structure of celestial bodies by measuring their static gravity field and tidal perturbations via radio science investigations. The determination of crucial parameters, including static gravity moments, Love numbers, and the rotational state of the planet, can be achieved by means of reliable techniques such as Doppler tracking of the spacecraft. By utilizing state-of-the-art radio systems, the technique enables measurements of the two-way line-of-sight velocity with remarkable precision, down to ~ 0.01 mm s^{-1} with a 60 s integration time (e.g., Iess et al. 2018, 2019; Durante et al. 2020; Parisi et al. 2020). In addition to gravity science methods, magnetic field measurements (e.g., Connerney et al. 2022) and planetary seismology (e.g., Fuller 2014; Panning et al. 2020; Mankovich & Fuller 2021) have been employed as well. Equally important are decisions regarding the spacecraft's trajectory around Uranus, which will significantly impact the kind of data it can collect, the quality of observations made, and the overall success in achieving the mission's scientific goals. This involves finding a balance between gaining insights into Uranus and its moons and ensuring the spacecraft's safety and functionality.

The Juno and Cassini missions to Jupiter and Saturn, respectively, have showcased the potential for repeated precise gravity measurements. Observations collected at close range to the planets have been pivotal in determining the internal density distribution and the depth of the visible zonal winds, as shown by Guillot et al. (2018), Kaspi et al. (2018), and Iess et al. (2019). The static component of the axially symmetric gravity field of giant planets can be attributed to two main factors: the uniform rotation of its deep interior (which is

---

[1] Retired

expressed in the even component of a spherical harmonic expansion) and the differential rotation of the winds (affecting both, but primarily the odd harmonics). The latter, arising from asymmetries in the hemispheres linked to atmospheric patterns, provides especially valuable insights into decoupling the two effects. The Juno gravity experiment provides a demonstration of such an approach (Kaspi et al. 2018). On the other hand, despite the smaller impact of differential rotation on the equatorially symmetric gravity field, its effect on even harmonics cannot be disregarded and requires careful calibration (Iess et al. 2019; Parisi et al. 2020; Kaspi et al. 2023).

To date, the only encounter between a spacecraft and Uranus occurred in 1986 January, when Voyager 2 performed a flyby of the planet, passing approximately 81,500 km above Uranus's cloud tops (Stone 1987). Radio science data were collected at closest approach and, in combination with Earth-based astrometry, resulted in the estimation of the degree-2 and degree-4 components of the zonal gravity field of Uranus (Jacobson 2014a). Recently, French et al. (2024) reported a new estimation for the same harmonics, through measurements of the apsidal precession and nodal regression rates of Uranus's rings. The estimates show significant differences from previous results and were derived by combining data between 1977 and 2006, from 31 Earth-based stellar occultations and three Voyager 2 occultations.

Uranus's zonal winds are powerful, with velocities reaching up to $200\,\mathrm{m\,s^{-1}}$ (Sromovsky et al. 2015), equivalent to 15% of the bulk rotation velocity at $60°$ latitude. Through the analysis of the excess on the degree-4 zonal harmonic as observed by Voyager 2 (Jacobson 2007), Kaspi et al. (2013) constrained the depth of the winds on Uranus. Employing a diverse set of interior models to eliminate the influence of the deep interior structure, their analysis provided evidence that the atmospheric circulation of Uranus is constrained to the initial 1000 km of the upper atmosphere. In more recent studies, Soyuer et al. (2020, 2022) obtained findings aligned with the earlier research, reinforcing the understanding that the scale height of Uranus's zonal winds does not exceed approximately 3% of the planet's mean radius. These critical insights into the zonal wind dynamics of Uranus provide valuable data for refining models and deepening our comprehension of the intricate atmospheric behavior on the ice giant. Nonetheless, the Voyager data alone do not establish a lower boundary for the depth of the winds. This essential science question remains unanswered, awaiting the arrival of an orbiter dedicated to studying Uranus in greater detail.

Unveiling the lower boundaries of Uranus's winds is only one of many critical steps toward comprehensively mapping its dynamical behavior. For instance, Uranus's tidal Love numbers capture periodic fluctuations in the planet's gravity field induced by its satellites' motion, and their values can constrain models of the interior. Stixrude et al. (2021) postulated that the planet's low luminosity and heat flow may be due to the presence of a growing frozen core, as opposed to mainstream adiabatic, inviscid models that predict a much larger luminosity than observed. The determination of the degree-2 Love number k_{22} holds great promise for determining whether or not much of Uranus's interior is solid, offering a quantum leap in our understanding of the planet.

In this work we present detailed numerical simulations of gravity science investigations at Uranus and their performance in terms of estimation of key parameters, such as the zonal spherical harmonics and tidal Love number. Section 2 will introduce possible mission scenarios, including candidate trajectories for the Uranus orbital phase and a description of the capabilities of state-of-the-art radio science instruments. In Section 3 we present the dynamical model used in the numerical simulations, including models for the rigid rotation and wind-induced components of Uranus's gravity field. Section 4 describes the data simulation and estimation process. In Section 5 we present the main results of the simulations, including expected measurement accuracies for the zonal spherical harmonics and Uranus's k_{22}. Section 6 presents our conclusions and discussion.

2. Uranus Orbiter and Probe: Possible Mission Scenarios

Over the past decade, several studies have been commissioned by NASA with the goal of returning to the Uranian system, including the Ice Giants Pre-Decadal Survey Mission Study (Hofstadter et al. 2017, 2019), the Uranus Orbiter and Probe Planetary Missions Concept Study (Simon et al. 2021), and the Planetary Science and Astrobiology Decadal Survey 2023–2032 (National Academies of Sciences, Engineering, and Medicine 2022). These reports explore the intricacies of planning an innovating yet realistic mission to Uranus and its moons, a task that extends far beyond the scope of this work. The vast majority of the findings strongly emphasize the need for a spacecraft to orbit Uranus for an extended period of time in order to be able to address the lingering science questions on ice giants. Accordingly, the mission scenarios presented in this work will consider a Uranus orbiter. Designing an interplanetary mission to the outer solar system requires a delicate balance of trade-offs, negotiations, and compromises. Distinct characteristics of the Uranus system pose unique challenges in mission planning and execution, such as extreme distance, harsh environmental conditions, and limited prior exploration. Some of the themes that will be discussed in this section center around the Uranus Orbiter and Probe (UOP) mission, while others will resonate with the broader context of all space missions.

When considering the constraints specific to the UOP mission, essential factors to address are the considerable distance between Earth and Uranus, which averages around 19 au, and the planet's unusual obliquity of $98°$. When the spacecraft transmits data back to Earth, the power available on board the spacecraft is severely limited, and the strength of the signal weakens proportionally with the square of the distance. Recent studies indicate that a power range between 350 and 450 W is necessary for efficient telecommunication (Simon et al. 2021). Therefore, the issue of available power on the spacecraft becomes crucial, and researchers have explored various options, including Next-Generation Radioisotope Thermoelectric Generators, solar power, and solar power stages (Simon et al. 2021). A different but related constraint involves the data transmission rates from the spacecraft, influenced, among other factors, by available power supplies, as well as the bandwidth and frequency capabilities of the radio system used for communication. While some instruments may demand large data volumes, others may require significantly smaller amounts. Gravity science, for instance, relies on the recorded radio carrier frequencies at the ground stations, requiring negligible data volume. The power consumption for science operations is directly related to the desired output level of the signal-to-noise ratio (S/N). The visibility of the

spacecraft from Earth, essential for Doppler tracking, is contingent on several factors, including the axial tilts of both Earth and Uranus. These circumstances create narrow time windows during which radio science investigations become feasible. The challenge in establishing consistent communication periods due to the interplay of planetary seasons was previously encountered by Voyager 2 and detailed in Stone (1987).

Previous studies have proposed possible trajectories for UOP, incorporating a Jupiter gravity assist for launch windows spanning from 2029 to 2032. These are considered the most advantageous options, optimized for both scientific exploration and efficiency. However, the landscape of mission planning has undergone significant changes, and current projections have pushed the anticipated launch window for these missions into the mid- to late 2030 s. This temporal shift brings forth a new set of considerations and complexities. A crucial aspect to consider is Uranus's season. During Voyager 2's flyby of Uranus, the planet was near its southern solstice, and only the southern hemispheres of Uranus's moons were illuminated and available for imaging. For this reason, there is a sense of urgency to revisit Uranus before the equinox in early 2050. However, mission planning considerations extend far beyond launch and cruise time. For instance, it is crucial to determine what the spacecraft will do upon reaching its destination: Will the spacecraft orbit Uranus outside of the rings while exploring and touring the moons? Or will it venture much closer to Uranus itself and inside the rings? When orbiting a planetary object, the spacecraft fires its main engines in order to change its velocity, in both magnitude and direction. Recent calculations assessing the available velocity change via maneuvers (ΔV) for a mission to Uranus indicate a budget of a few kilometers per second (R. Karimi, personal communication). However, when factoring in the costs associated with the Uranus Orbit Insertion (UOI) maneuver, moon touring, and probe release, the remaining ΔV allocated for the gravity/magnetometer phase, for which proximity to the planet is essential, may be reduced to a few hundreds of meters per second.

Time represents another constrained resource, with the mission set to meet all primary science objectives within the nominal duration. Transitioning between equatorial (advantageous for the moon tour) and moderately inclined orbits (advantageous for gravity and magnetometer science) can utilize the outer satellites of Uranus if enough time is involved (over a year), impacting the mission's time line and objectives. Efforts to hasten the journey to Uranus necessitate employing a larger ΔV to enter orbit swiftly or exploring newer technologies like aerocapture (e.g., Dutta et al. 2024). However, relying on the latter may be perceived as risky and could escalate mission costs significantly.

Finally, gravity science orbits that require the spacecraft to dive between the rings and the upper atmosphere of Uranus present a significant challenge owing to the inherent complexity of predicting potential risks encountered in this uncharted region. Cassini discovered a less hostile ring environment at Saturn than previously anticipated, but there is no guarantee that this will be the case for UOP, especially considering the remarkable differences between the two ring systems. On the other hand, venturing too close to the upper atmosphere of a gaseous planet like Uranus introduces its own uncertainties surrounding the density of the upper atmosphere. The most

promising strategy seems to involve identifying a strategic orbital location: a position distant enough from densely populated ring regions while maintaining a safe distance from the poorly known upper atmosphere. Present estimates identify this region as roughly in the range from 1.08 to 1.11 Uranus radii (R_U; Hofstadter et al. 2019).

2.1. Gravity Science Trajectories

In an internal study of possible missions to Uranus, several orbital tours within the system were developed to try to meet all the science objectives (including nongravity ones) while keeping within what were considered reasonable mission constraints such as available fuel, time in orbit, and avoiding hazardous regions for the spacecraft. We selected three of those trajectories to represent the three main classes: trajectories that assume that it is unsafe to fly the spacecraft between the rings and the planet, so there are no close periapses over the equator; a Cassini-like trajectory that does have close pericenters near the equator; and a trajectory that allows close pericenters over the equator but also enters a more Juno-like orbit with a quasi-polar inclination. For each of those three trajectories, we also considered the case where the periapses were visible from Earth and the case where they occurred behind the planet as seen from Earth, degrading our information on the gravity field closest to the planet. This allowed us to explore the impact of pericenter altitude, latitude, longitude, and visibility, as well as orbital inclination, on our ability to determine the gravity field of Uranus. On the other hand, we maintained certain parameters consistent across all cases: a fixed number of pericenters (8), a fixed spacecraft orbital period (90 days), and the same Uranus season throughout the mission duration (between 2049 June and 2051 July). Realistic orbits are characterized by a high level of eccentricity ($\sim$0.98), likely representing a viable option owing to the limited ΔV. For reference, a circular orbit at $1.1R_U$ would require up to 20 times the budgeted fuel consumption with chemical propulsion systems. This uniformity ensured a common baseline for our investigations, facilitating a more comprehensive and rigorous analysis of the varying trajectories' effects on the gravity field retrieval process.

The first case (Trajectory 1) features spacecraft equator crossings outside of the rings (purple lines in Figure 1(a)). The goal is to keep the spacecraft outside of the region characterized by the highest risks associated with ring hazard; hence, the pericenters must occur at high latitudes ($\sim$62° S) and, in this example, are confined to the southern hemisphere (Figure 1(b)). Pericenter altitudes are also higher ($\sim$5150 km), in order to ensure that the ascending and descending nodes of the spacecraft trajectory with respect to Uranus's equatorial plane are located at least $2R_U$ away from the center of the planet. Conversely, pericenter longitudes are quite spread out because Uranus rotates quickly underneath the ground tracks. The inclination of the spacecraft orbit is 115°. The orbiter–Uranus–Earth (OUE) angle is <105°, which implies that all pericenters are visible from Earth, without the spacecraft being occulted by Uranus.

Trajectory 2 belongs to a different class of trajectories, whose equator crossings take place between the innermost ring of Uranus and the top of the troposphere (green lines of Figure 1(a)). For reference, the inner boundary of the rings has been chosen to align with the extension of the ζ ring, down to roughly 7000 km altitude (de Pater et al. 2006). To successfully
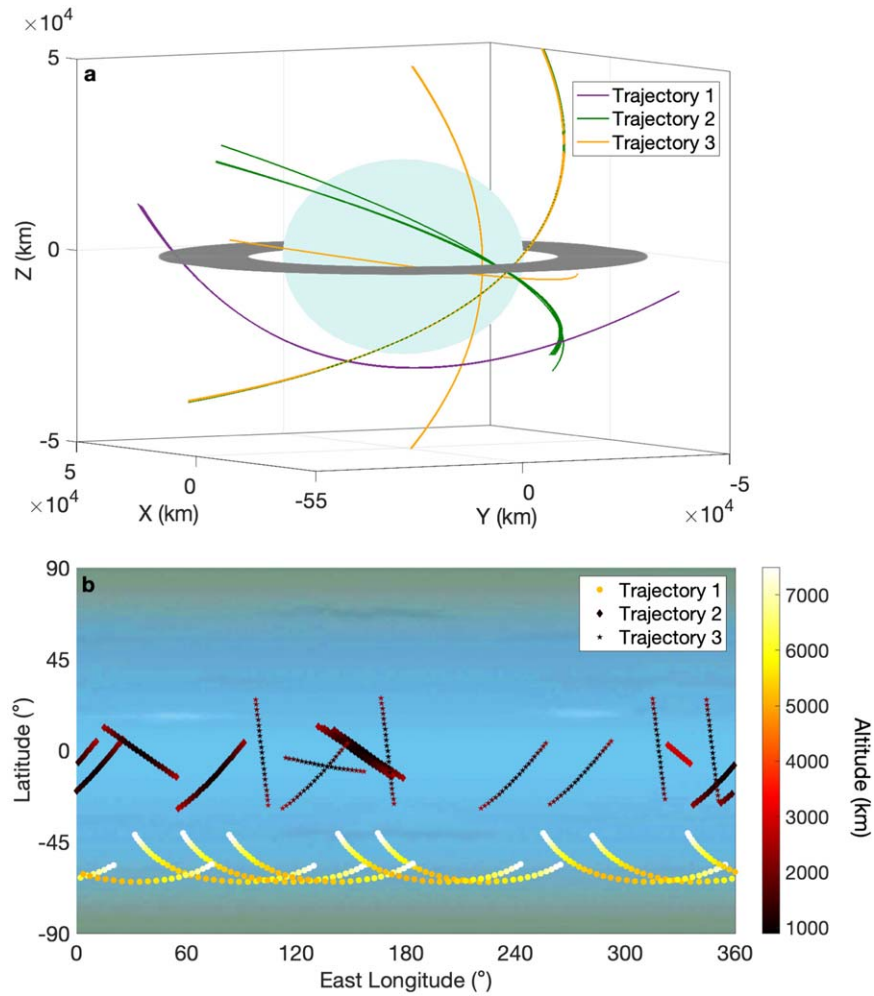
Figure 1. Spacecraft ground tracks for ±20 minutes around each closest approach to Uranus for Trajectories 1, 2, and 3. Panel (a) shows the spacecraft pericenters outside (Trajectory 1) and inside (Trajectories 2 and 3) the ring region (gray shaded area). The orbits are plotted with respect to a nonrotating reference frame that is fixed with Uranus (the z-axis is aligned with Uranus's rotation axis, and xy is the equatorial plane) from Archinal et al. (2018). The eight orbits for each trajectory case are shown, though they sometimes overlap in the chosen reference frame. Panel (b) shows the ground tracks with respect to Uranus's rotating frame (Archinal et al. 2018) for the three trajectories. The tracks show the spacecraft altitude for 20 minutes around closest approach (trajectory ticks are generated every 60 s). The spacecraft altitude over Uranus's atmosphere is calculated considering the 1-bar shape from Helled et al. (2010). Background image credit: NASA/JPL/Hastings-Trew/Thomas.

navigate the spacecraft through this narrow space, the pericenter altitude should be low enough to steer clear of Uranus's ring particles, while also being high enough to avoid atmospheric-drag-induced torque (Parisi 2023). Two spacecraft maneuvers occur after the third and fifth pericenters, respectively, and target the closest approach latitudes. This is accomplished by tweaking the orbital inclination of the spacecraft, which increases from 140° to 150° after the first maneuver. As a result, the pericenter latitude changes from ∼12° S to ∼0°. The average altitude over Uranus's troposphere at closest approach is ∼1000 km (Figure 1(b)), with the exception of the pass right after the first maneuver, whose minimum elevation is ∼2800 km. Unlike the previous case, the OUE angle is ∼160°, resulting in the spacecraft routinely disappearing behind the planet for intervals of about 45 minutes centered around its closest points. While this scenario provides ample opportunities for radio occultations to study the planet's ionosphere and neutral atmosphere, it disrupts the direct line-of-sight communication between the spacecraft and ground stations, and the impact on gravity field recovery will be addressed in following sections.

Trajectory 3 (yellow lines in Figure 1(a)) closely resembles the previous case, with a significant difference. During the second maneuver (occurring just after pericenter 4 in this case), the thrusters are fired to change the inclination to 90°. This slight variation is crucial, as it results in a wider range of latitudes covered by the spacecraft during its last four close encounters with the planet (as shown in Figure 1(b)). This is typically a favorable scenario for the estimation of zonal harmonics. Other parameters, including altitude and latitude of pericenter and OUE angle (presence of occultations lasting ∼45 minutes), are unaffected.

2.2. The Radio Science Instrument

In order to conduct a successful interplanetary radio science experiment, a coordinated effort between the ground and space segments is essential. The ground segment relies on NASA's Deep Space Network (DSN), featuring 34 and 70 m antennas suitable for gravity science applications. The space segment typically consists of X- (7.2–8.4 GHz) and Ka-band (32.5–34.0 GHz) transponders carried aboard the spacecraft, which establish coherent and highly stable radio links with DSN

stations. The space segment includes also the spacecraft's High Gain Antenna (HGA), which ensures high levels of S/N on the radio signals. For the UOP simulations described in this work, we assume that the orbiter is equipped with state-of-the-art radio science instrumentation, comparable to that flying on NASA's Juno and ESA's BepiColombo and JUICE missions (De Tiberis et al. 2011; Asmar et al. 2017; Cappuccio et al. 2020). The standard configuration for gravity science experiments involves two-way links: the ground station transmits radio signals to the spacecraft, which receives and retransmits them back to the originating antenna. Two-way experiments are referenced to the frequency standards at the DSN complexes (hydrogen masers). Consequently, there is no gravity science requirement for the spacecraft to be equipped with an Ultra Stable Oscillator (USO), as the standard frequency is established and maintained from the ground. However, a USO is crucial for the execution of the radio occultation portion of the radio science experiment.

Employing multifrequency links for gravity science experiments presents several advantages. Arguably, one of the most significant is the capability to calibrate out 75%–100% of the plasma noise from dual-band and triple-band links, respectively (Mariotti & Tortora 2013). Plasma behaves as a dispersive medium, causing the signal phase to advance compared to a signal that travels in vacuum. This advancement is proportional to the electron density and inversely proportional to the square of the signal frequency. Consequently, by combining two or more links, it is possible to isolate the portion of the Doppler shift attributed to the presence of plasma. It also follows that Ka-band links, characterized by higher frequencies, are intrinsically more robust to plasma noise than X-band signals. Asmar et al. (2005) report a plasma noise level on X-band observables up to one order of magnitude higher when compared to Ka band, for Sun–Earth–probe (SEP) angles between $10°$ and $90°$. The impact of plasma noise on the Doppler signal becomes particularly significant during the time period when the SEP angle is very small ($<10°$) and the Sun is located between the ground stations and the spacecraft (solar conjunction). On the other hand, when the spacecraft is near solar opposition and the Sun is behind Earth, noise due to solar interference is at a minimum (Asmar et al. 2005). Other possible sources of plasma noise are Earth's ionosphere, which is routinely calibrated using models based on Global Positioning System (GPS) observations (Richter 2000), and plasma-rich regions that are local to the Uranian system (e.g., Uranus's own ionosphere during grazing occultations). In addition, employing Ka-band radio carriers for the radio system also provides approximately four times the data volume compared to X band.

Troposphere noise is a principal contributor to disturbances in Doppler measurements, arising from the dry and wet components of Earth's atmosphere. Notably, the wet component is extremely unpredictable and exerts a significant influence on the radio signal's propagation, and modeling the effect of water vapor particles suspended within this medium is challenging. However, troposphere fluctuations do not depend on the signal frequency and affect X band and Ka band equally. There are two sources of calibrations for troposphere noise: Tracking System Analytical Calibrations, which rely on models of the troposphere and struggle with calibrating the rapidly changing water vapor content, and Advanced Water Vapor Radiometer (AWVR) calibrations. AWVRs are units placed in the proximity of deep-space antennas, capable of directly measuring the water vapor content along the nadir direction. An extensive analysis of Juno gravity data revealed that AWVR calibrations are capable of abating the noise level on 60 s Doppler data by as much as 75% (Buccino et al. 2021). Currently, AWVRs are available only in the proximity of Goldstone's DSS-25, but plans for embedding radiometers within deep-space antennas are being considered by NASA (Tanner et al. 2021). Lastly, the Allan deviation of frequency fluctuations due to thermal noise is proportional to $\left(\frac{1}{S/N}\right)^{-1/2}$; therefore, higher S/N values are preferred. Gravity science experiments commonly employ the spacecraft's HGA, which remains Earth pointed for the duration of the experiment and ensures average levels of S/N of ~40 dB-Hz using 34 m dishes. Under these circumstances, thermal noise is rarely the dominant noise source. However, successful radio science experiments have operated within lower S/N ranges of 10–30 dB-Hz, involving the use of Medium or Low Gain Antennas (e.g., Parisi et al. 2023) and higher regimes of thermal noise. Recent advancements in radio tracking experiments include the possibility of achieving successful phase lock between the spacecraft transponder and ground antennas, even at an S/N as low as 4 dB-Hz (Buccino et al. 2023).

Overall, our assumptions regarding the noise level in Doppler measurements for the Uranus orbiter are grounded in the extensive data collected and analyzed by the Juno science team (Durante et al. 2020; Parisi et al. 2020; Buccino et al. 2021). An average rms noise level of 0.01 mm s^{-1} is assumed for range-rate measurements collected using DSS-25, for an integration time of 60 s typical of gravity experiments (Iess et al. 2018; Durante et al. 2020; Buccino et al. 2021). Range-rate represents the rate of change of the spacecraft linear distance to Earth (line-of-sight velocity) and is measured directly by recording the Doppler shift on the radio carrier. For data collected at the Madrid and Canberra DSN complexes, the noise level increases to 0.02 mm s^{-1} at 60 s. We also timed the gravity passes so that continuous Doppler tracking of the spacecraft is available for ±3 hr around closest approach (except during Uranus occultations) while the spacecraft is in gravity science attitude. All DSN complexes are used to collect Doppler data at pericenter, depending on their visibility at the reference epoch.

3. Dynamical Model of the Uranian System

The dynamical model is an umbrella term that encompasses current information about the surroundings of a spacecraft in orbit around a celestial body, in this case Uranus. This includes gravitational accelerations (e.g., static gravity field coefficients for Uranus and its moons, tidal perturbations, internal oscillations) and nongravitational perturbations such as solar radiation pressure, thermal emission, and planetary albedo. By integrating these various forces, the dynamical model provides a nuanced representation of the factors affecting the spacecraft's trajectory within the Uranian system.

3.1. Zonal Gravity Field

The gravity field measurements obtained from the Voyager 2 mission revealed a range of possible interior structures, allowing for an array of theoretical models that could potentially explain the observed zonally symmetric harmonic coefficients. As noted earlier, one of the components of the gravitational potential stems from the planet's internal density
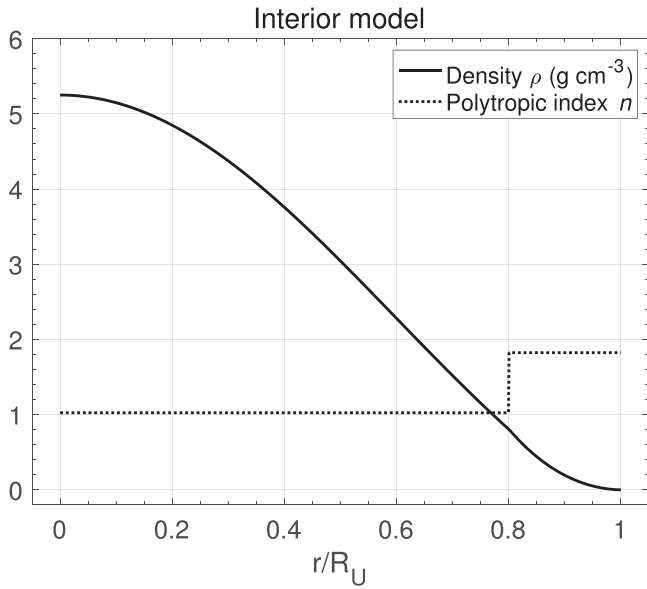
Figure 2. Interior model of Uranus using composite polytropes with interface at $0.8R_U$. The density profile and the adiabatic index are shown as a function of the fractional radius.

Figure 3. Longitudinal sections of Uranus's wind models in m s^{-1} featuring (a) shallow and (b) deep winds, as a function of fractional radius.

distribution (which is, generally, considered hydrostatic), which is affected by the rapid rotation and associated with the centrifugal force that flattens the planetary figure. This, in turn, generates deviations from sphericity in the planet's gravitational field that are symmetric with respect to its equatorial plane. These manifest as even-degree spherical harmonics, with their magnitude diminishing exponentially with the harmonic degree.

For reference, Figure 2 shows a piecewise polytropic Uranus interior model that fits the external gravitational potential from Jacobson (2014a), assuming that the estimated coefficients are entirely due to rigid rotation. The density is assumed to be continuous, but a break in polytropic index (n) is enforced at $0.8R_U$, with inner and outer polytropic indices chosen to match $J_2 \times 10^6 = 3510.7$ and $J_4 \times 10^6 = -34.2$. The polytropic index relates the pressure (p) and density (ρ) profiles:

$$p \propto \rho^{1+\frac{1}{n}}. \qquad (1)$$

The shape and gravity field were calculated using fourth-order theory of figures (Mankovich et al. 2019; Mankovich & Fuller 2021). This interior model is used to explain the measured gravity field coefficients J_2 and J_4, predict the higher degree harmonics J_6 and J_8, and integrate the spacecraft trajectory discussed below (Section 4). The model is also used to account for the hydrostatic background density when solving the thermal wind equation described in the next paragraph.

The second component of the gravity field arises from the differential rotation of the visible zonal winds, superimposed on the rigid rotation of the planet's deep interior. Uranus's atmosphere can be regarded to be, to first order, in a state of thermal wind balance, with pressure gradients balanced by the Coriolis force (Kaspi et al. 2013):

$$2\mathbf{\Omega} \cdot \nabla(\tilde{\rho}\mathbf{v}) = \nabla\rho' \times \mathbf{g}, \qquad (2)$$

where $\mathbf{\Omega}$ is the planet's rotation rate, $\tilde{\rho}$ is the hydrostatic density, $\mathbf{v}$ is the velocity vector, ρ' are the density perturbations due to winds, and $\mathbf{g}$ is the radial gravity vector. If the three-dimensional velocity field is known, we can calculate the
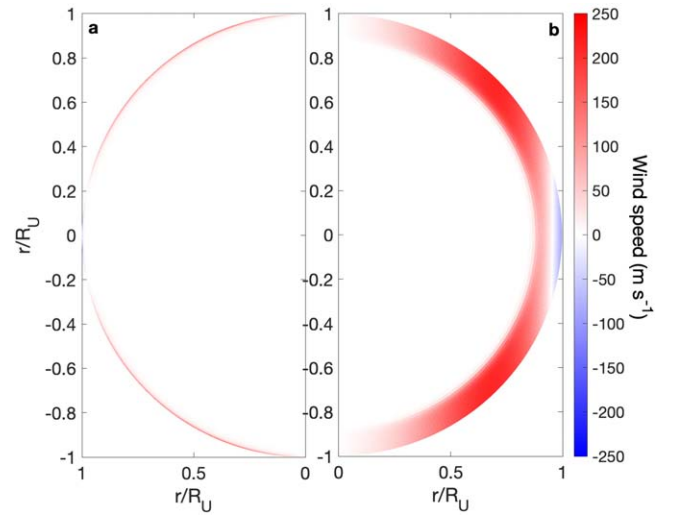
density perturbations if a reference state ($\tilde{\rho}$, $\mathbf{g}$) can be reasonably assumed.

For our Uranus exercise, we assume $\Omega = 1.0124 \times 10^{-4}$ rad s^{-1}, consistent with the rotation period of $17^h14^m24^s$ reported in Archinal et al. (2018). In reality, Uranus's rotation rate is poorly determined, and the current uncertainty on the prime meridian is over a complete rotation (Archinal et al. 2018). Desch et al. (1986) used Voyager's radioastronomy and magnetometetry observations to measure the parameter, whose value is also reported in the IAU report. Using a different approach that minimizes the dynamical heights, Helled et al. (2010) found that in order to fit Voyager's occultation radii and gravitational parameters, Uranus must rotate with a period of ∼16.58 hr. Therefore, to properly account for this level of uncertainty, we are taking an agnostic stance for our simulations and allow the rotation rate value to span 100% of its nominal value.

Differently, $\tilde{\rho}$ and $\mathbf{g}$ are derived from the reference model in Figure 2. The last piece of the puzzle needed to solve Equation (2) for ρ' is the velocity field $\mathbf{v}$. Updated and improved surface wind speed measurements have been obtained by Sromovsky et al. (2015) using near-infrared imaging of Uranus between 2012 and 2014. As a result, a composite zonal wind profile for Uranus is available as a function of latitude (Figure 15 of Sromovsky et al. 2015). We use the data as surface boundary conditions to construct two models of Uranus's deep circulation (Figure 3). One (panel (a)) is obtained by propagating the surface winds along coaxial cylinders aligned with Uranus spin axis to ∼100 km within the atmosphere. The other profile (panel (b)) shows a similar vertical alignment to the rotation axis but deeper atmospheric dynamics (∼3000 km). If we accept the 1000 km upper limit on the wind depth proposed by Kaspi et al. (2013), the actual circulation pattern of Uranus would likely resemble an intermediate scenario between these two cases. We assume azimuthal symmetry and replicate the vertical section shown in Figure 3 for each value of longitude. We then numerically integrate Equation (2) to obtain the density perturbation map generated by Uranus's winds. The chosen resolution is 1° in latitude and longitude and five vertical levels per scale height.
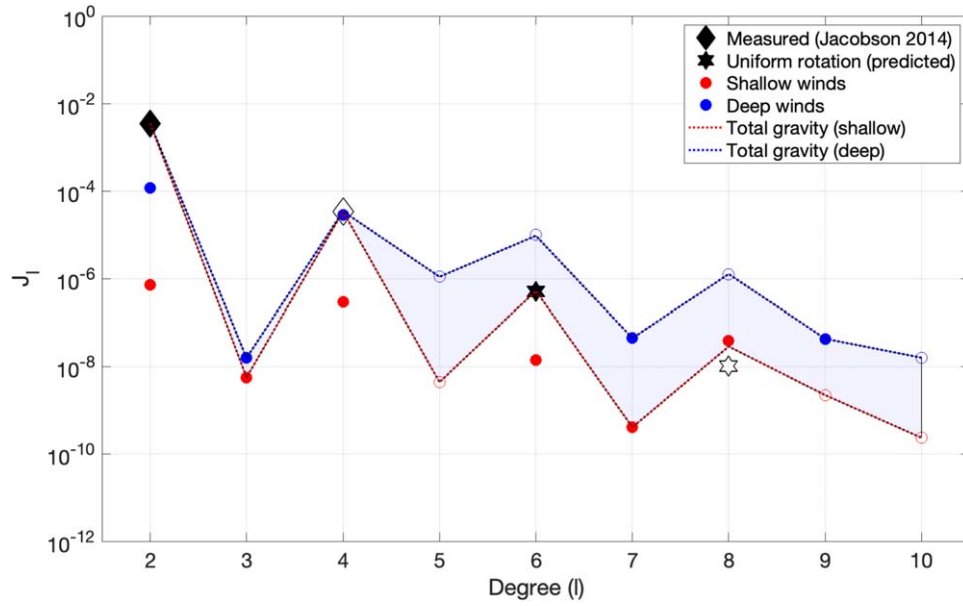
Figure 4. Uranus's gravity field spectrum, including different contributions: measured coefficients (black diamonds), predicted effect of solid-body rotation (black stars), and predicted wind-induced gravity signal for shallow (red circles) and deep wind (blue circles) models. Filled and open symbols represent positive and negative values, respectively. The shaded area represents the sum of the uniform and differential rotation contributions and shows the possible range for high-order gravity moments, between the deep (blue dotted line) and shallow (red dotted line) cases.

The density fluctuations caused by Uranus's zonal flows impact the planet's external gravitational potential in a way that is also azimuthally symmetric. The wind-induced gravity signal carried by zonal harmonics of degree l can be calculated as (Parisi et al. 2020)

$$\Delta J_l = \frac{1}{M_U R_U^l} \int_0^{R_U} r^{2+l} dr \int_0^{2\pi} d\phi \int_{-1}^1 P_l(\cos\theta)\rho' d\mu, \quad (3)$$

where M_U is the mass of Uranus, r is the radial coordinate, ϕ and θ are longitude and latitude, respectively, and P_l is the Legendre polynomial of degree l. Figure 4 shows the different contributions to Uranus's zonal gravity field. A combination of Voyager 2 radio science and ground-based astrometric data was used to determine the values of J_2 and J_4 with uncertainties of 3×10^{-7} and 4×10^{-7}, respectively (Jacobson 2014a). Predictions for the uniform rotation component for degrees 6 and 8 are based on the interior model of Figure 2. Predictions for the wind-induced gravity signal are also available for the shallow and deep circulation models from Equation (3). It is important to emphasize that the strong influence of the symmetric component in Uranus's wind profile primarily affects the even harmonics. Nevertheless, odd harmonics are present, as illustrated in Figure 4, though characterized by substantially smaller magnitudes. These coefficients arise as a result of subtle asymmetries observed in Uranus's wind profile versus latitude, as documented in Sromovsky et al. (2015). Finally, the total expected gravity spectra from the two scenarios are represented. These curves provide a practical prediction for Uranus's gravity field, indicating their expected magnitude as compared to the expected accuracies in the coefficient estimation.

3.2. Tidal Perturbations

The Love numbers k_{lm} (l is the degree, m is the order) measure the elastic tidal response of the gravity field of Uranus to the presence of its satellites. They are defined as the ratio between gravity field perturbations caused by tidal forces and the applied tidal gravitational potential (neglecting, to first order, coupling of potential between different degrees). The leading degree and order of the tidal response are $l = m = 2$ (Idini & Stevenson 2021; Stixrude et al. 2021), which means that the equipotential surfaces deform into ellipsoids, with the major axis aligned with the Uranus–moon direction in the limit of an equilibrium tide.

Depending on Uranus's composition and internal structure, the response will vary in accordance with the value of k_{22}. Stixrude et al. (2021) provide a possible range of values between 0.28 and 0.36, wherein the lower and higher ends of the spectrum are associated with models featuring a solid and fluid core, respectively. Additionally, this theory accurately predicts levels of tidal dissipation consistent with calculations derived from the orbits of Uranus's main satellites. On the other hand, a recent work by Nimmo (2023) argues that geologic evidence suggests a much more dissipative Uranus, perhaps through the action of resonance locking between moon orbits and Uranus normal modes, as seems to be the case at Saturn.

The magnitude of the external forcing on the planet can be quantified by the tidal parameter (Rappaport et al. 1997):

$$q_t = -3\frac{M_p}{M_U}\left(\frac{R_U}{a}\right)^3, \quad (4)$$

where M_p is the mass of the perturbing body and a is the semimajor axis of the perturber's orbit. Figure 5 shows the value of $|q_t|$ for the satellite systems of the four giant planets. Unsurprisingly, Io stands out in terms of tidal power owing to the significant stresses imposed by the gravitational interactions with Jupiter (and vice versa). We observe that Ariel ranks third in terms of tidal forcing, behind Jupiter's Io and Neptune's Triton. Uranus's tides, as well as those raised on any gaseous planet, can be satellite dependent (Notaro et al. 2019), with the planet being characterized by different values of Love numbers for each
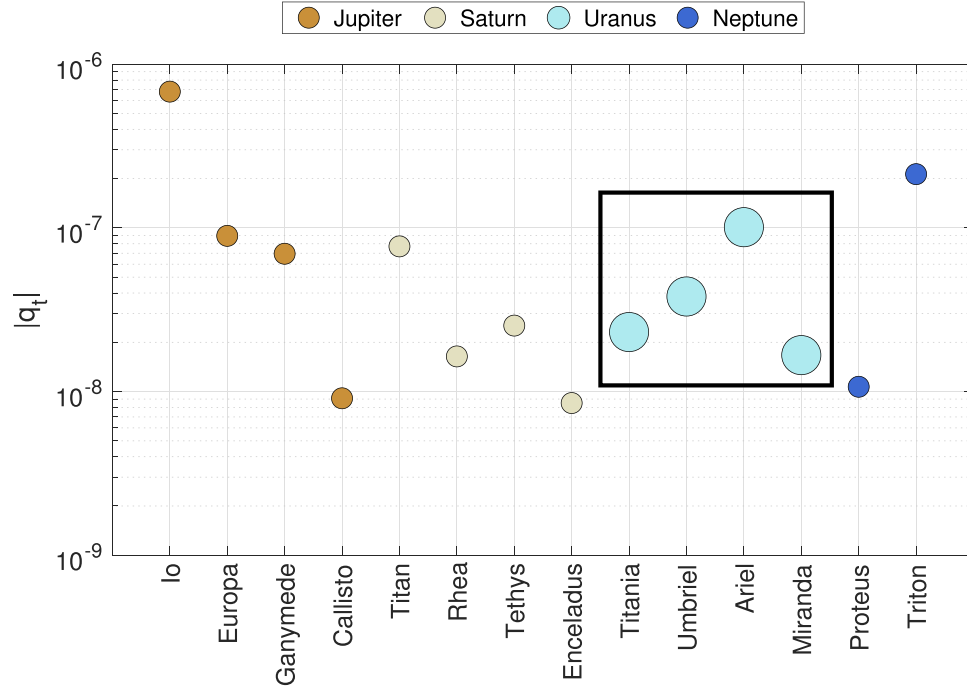
Figure 5. Magnitude of the tidal parameter calculated for the four giant planets and their major satellites. The color code follows the planets' color palettes, while the black box highlights the object of our study: Uranus.

satellite. However, other Uranian satellites exert a much smaller tidal forcing on Uranus; therefore, we can assume that Ariel is the only body capable of raising detectable tides on the planet.

Since part of this work is focused on assessing the detectability of Uranus's k_{22}, this represents an encouraging result. However, the ability to comprehensively capture Uranus's tidal response depends on several additional factors, including the number of pericenters, spacecraft altitude over the cloud tops, and samples of longitudinal phase with respect to the tidal bulge. The geometries of the observations are reported in Figure 6 for the three different orbits. Each point indicates the relative position of the spacecraft with respect to the tidal ellipsoid for each of the eight pericenters. Phase 0 represents the direction of Ariel with respect to Uranus. Despite the constant value of eccentricity, the epochs of the pericenter passes can vary by as much as 24 hr among different trajectory cases, due to slight differences in the selected UOI maneuvers, as well as impulsive burns used to change the orbital inclination and pericenter latitudes. Because Ariel completes a revolution around Uranus in 2.52 Earth days, the spacecraft phase angles can vary by as much as 140° among the different trajectories.

We note that all orbits are characterized by a rather uniform spread of phase angles, which is advantageous for a good estimation of Uranus's k_{22}. However, the coverage improves with Trajectories 2 and 3 as compared to Trajectory 1; therefore, it is reasonable to expect a better outcome for these cases, given that they are also characterized by lower pericenter altitudes (Figure 1). Love numbers of higher degree and order (e.g., k_{31}, k_{33}) are not expected to be detectable, as their effects decrease sharply with distance, but the impact on the overall estimation process is nonetheless accounted for (see Section 4).

3.3. Piecewise Constant Accelerations and Other Parameters

The amplitude of normal modes on Uranus and ice giants in general is still unknown (Friedson 2020). Ground-based
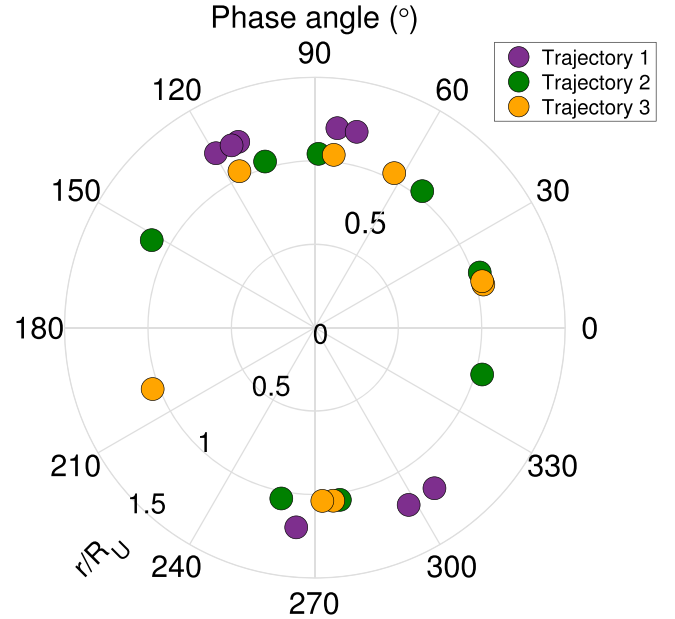

Figure 6. Phase angles between the spacecraft direction and the Ariel direction with respect to Uranus, at the time of each closest approach, for the three trajectories considered in this study. All trajectories sample a wide range of phase angles, which is optimal for determining the tidal Love number.

observations of Neptune set an upper limit to the surface amplitude of internal oscillations at approximately 40 cm s^{-1} (Rowe et al. 2017). Nonetheless, it is plausible that ice giants may harbor modes of lesser intensity compared to those observed in Jupiter and Saturn (Markham et al. 2020; Durante et al. 2022). Interestingly, French et al. (2024) suggest that a mode with azimuthal order 3 was observed in the γ-ring, potentially indicating a resonance with an internal planetary oscillation. While this study does not aim to address the detection of normal modes through radiometric measurements,

the presence of unmodeled physical phenomena may potentially lead to aliasing of the solved-for parameters. Therefore, the potential effect on Doppler measurements from the accelerations experienced by the spacecraft due to Uranus's oscillations must be considered.

We address normal mode interference by incorporating piecewise constant accelerations on the spacecraft, following the approach in Iess et al. (2019) and Durante et al. (2020). Within approximately 2 hr of the spacecraft's closest approach to the planet, we implement a random time series for the three components of the accelerations. These are calculated along the x-direction (aligned with the spacecraft–Uranus direction), the z-direction (perpendicular to the spacecraft's orbital plane), and the y-direction (completing the triad). Each segment of this time series spans a duration of 10 minutes, forming individual batches (12 for each pericenter) wherein the acceleration remains constant in amplitude and direction. The disturbances experienced by the Juno and Cassini spacecraft due to internal oscillations of Jupiter and Saturn exhibited significant differences in magnitude, with the latter approximately 20 times larger. Considering this variability, our Uranus simulations account for two distinct scenarios yielding different outcomes. The first scenario, Jupiter-like, assumes a maximum value of 2×10^{-8} ms^{-2} for these accelerations, as detailed in Durante et al. (2020). The second scenario, Saturn-like, uses instead an increased value of 4×10^{-7} ms^{-2} based on Iess et al. (2019). Notably, these acceleration levels were observed at altitudes over the 1-bar surfaces of Jupiter and Saturn, averaging around 4000 and 3000 km, respectively. The three Uranus trajectories are characterized by altitudes ranging from 1000 to 5000 km. However, the magnitude of the piecewise constant accelerations was kept consistent regardless of pericenter altitude. Consequently, our approach is conservative and may lean toward somewhat pessimistic results, particularly for the high-altitude case (Trajectory 1). On the other hand, this approach allows us to reasonably accommodate any uncertainties in the parameters of interest arising from our limited understanding of Uranus's normal modes.

The dynamical model also includes the masses of the Uranian rings. Current estimates indicate that the ϵ ring has a mass of around 10^{16} kg (Esposito & Colwell 1989), while the α and β rings each have a mass of approximately 10^{15} kg (Chiang & Culter 2003). Because of the significant uncertainties associated with these parameters, we allow these parameters to vary by as much as 100% of their nominal values.

The magnitude of nongravitational accelerations experienced by the spacecraft is linked to the shape of its components. In our analysis, we have utilized a simplified spacecraft model primarily based on Cassini. Our dynamical model takes into account various forces such as the planet's albedo, thermal emission, and solar radiation pressure. Furthermore, due to the proximity to Uranus's 1-bar surface during the close pericenters, we have considered the impact of atmospheric drag on the spacecraft's trajectory. The upper atmosphere of Uranus is composed mainly of hydrogen and helium, with the methane mostly condensed out at the altitudes considered in the study. Due to the limited availability of direct measurements, determining the exact density of the upper atmosphere of Uranus is challenging. The neutral density diminishes exponentially with increasing altitude, and the uppermost layers gradually transition into what is known as the exosphere, characterized by extremely low densities. In our efforts to characterize Uranus's atmosphere, we utilize an exponential decay for the density profile, with a base density of 10^{-14} kg cm^{-3} and a scale height of 400 km for a reference altitude of 1000 km over the 1-bar level, based on observations reported in Strobel et al. (1991). Similarly to other unknown parameters, we allow the value of the base density to vary significantly in our simulations (see Section 4). Our simulations reveal that nongravitational accelerations (with the exception of atmospheric drag) during the Uranus tour consistently remain below 10^{-13} km s^{-2}, likely below the radio science instrumentation detection threshold. Nevertheless, it is important to account for these relatively minor factors when considering the overall dynamics of the spacecraft in its orbital environment.

Table 1 provides a summary of the dynamical model utilized for integrating the trajectory of the spacecraft as described in the previous subsections. The planets' state vector within the solar system and the positions of Uranus's satellites are derived from the Jet Propulsion Laboratory (JPL) planetary ephemeris DE440 (Park et al. 2021) and satellite ephemerides URA111 (Jacobson 2014b). Reference values for Uranus's pole motion, gravity field, and degree-2 Love number are sourced from Jacobson (2014a), Archinal et al. (2018), and Stixrude et al. (2021), respectively.

4. The Simulated Orbit Determination Process

Orbit determination is a powerful technique used for determining the trajectory of objects in space relative to a reference frame. It involves solving the equations of motion starting from the initial conditions representing the state of a body at a reference epoch. The initial state traditionally consists of position and velocity vectors, but more often than not the solution also includes parameters defining the dynamical model (e.g., the planet's gravity field coefficients and Love numbers). The collection of these parameters is called the solved-for vector. If the initial state and the dynamical model described in the previous section were known with infinite precision, the future evolution of the spacecraft trajectory could be predicted exactly, provided that the governing differential equations were known. However, uncertainties in initial conditions, dynamical model constants, and observation errors complicate the process. Observations from Earth stations, measuring range (linear distance between the spacecraft and Earth) and range-rate typically used for gravity science experiments, are subject to errors, requiring statistical methods for the estimation of the solved-for vector.

Despite optimization, estimated trajectories often deviate from real trajectories owing to various errors, requiring constant updates. The least-squares method consists of selecting (from infinite possibilities) the initial state for the solved-for parameters that minimizes these deviations. In addition, if a priori knowledge of the spacecraft state is available, it can be used as a constraint that anchors the new estimate of the solved-for vector to preexisting values (for instance, gravity field coefficients of a body as determined by a previous mission). The rigidity of the constraint is defined by the a priori uncertainties.

The process described above was carried out numerically using JPL's Mission Analysis, Operations, and Navigation Toolkit Environment (MONTE; Evans et al. 2018). In addition to X- and Ka-band 60 s range-rate data, we also included X-band range data and X/Ka-band three-way range-rate data. The former were simulated with a count time of 300 s and

Table 1
Dynamical Model of the Uranian System Used to Integrate the UOP Trajectory

Type	Dynamical Model Parameters	Reference Value
Gravitational accelerations	GM of the Sun and planets	Park et al. (2021)
	Uranus's rotation and pole motion	Archinal et al. (2018)
	Uranus's J_2 and J_4	Jacobson (2014a)
	Uranus's k_{22}	Stixrude et al. (2021)
	GM of Uranus's satellites	Jacobson (2014b)
	GM of Uranus's rings	Esposito & Colwell (1989)
		Chiang & Culter (2003)
Nongravitational accelerations	Solar radiation pressure	
	Uranus's albedo	Pearl et al. (1990)
	Uranus's thermal emission	
	Atmospheric drag	Strobel et al. (1991)

Table 2
List of Estimated and Consider Parameters for the Covariance Analysis

Type	Solved-for Parameters	A Priori Uncertainties
Local	Spacecraft state vector ($\times 6$)	10^{10} km/10^0 km s^{-1}
	Piecewise constant accelerations (normal modes) ($\times 36$)	$(2–40) \times 10^{-11}$ km s^{-2}
Global	Uranus system barycenter GM ($\times 1$)	10^1 km^3 s^{-2}
	Uranus's R.A. and decl. ($\times 4$)	10^0 rad/10^0 rad s^{-1}
	Uranus's J_2–J_{25} ($\times 24$)	10^0
	Uranus's degree-2 tesseral field ($\times 4$)	10^0
	Real part of Uranus's k_{22} ($\times 1$)	10^0
Consider	State vector and GM of main satellites ($\times 7$ each)	10^1 km/10^{-3} km s^{-1}/10^1 km^3 s^{-2}
	Uranus's rotation rate ($\times 1$)	10^{-4} rad s^{-1}
	Real part of Uranus's k_{31}, k_{33}, k_{42}, and k_{44} ($\times 4$)	5×10^{-1}
	Albedo scale factor ($\times 1$)	2×10^{-1}
	Thermal emission scale factor ($\times 1$)	2×10^{-1}
	Solar radiation pressure scale factor ($\times 1$)	2×10^{-1}
	Atmosphere base density ($\times 1$)	10^{-14} kg cm^{-3}
	GM of Uranus's rings ($\times 1$)	10^{-3} km^3 s^{-2}

accuracies around 20 cm (Park et al. 2021), although it has been shown that these measurements can potentially reach accuracies as low as 1 cm for integration times of the order of seconds, with more advanced ranging systems (Cappuccio et al. 2020). The three-way range-rate data were characterized by a noise similar to their two-way counterpart and were used during gaps in the preferred data type due to station hand-overs. The inclusion of data points where the uplink and downlink stations differ typically requires either careful calibration of possible clock biases present among different DSN stations or estimation of additional parameters related to this effect. On the one hand, covering longer periods of time with available Doppler data has a beneficial effect on parameter estimation. On the other hand, the estimation of parameters associated with a clock bias can partially counteract this beneficial effect. We note that the addition of these auxiliary data points improves the estimation accuracies of gravity field and tidal parameters by a maximum of 15%. We chose to show the results using two-way data only in Section 5, as a representative case. Finally, due to the significant influence of the troposphere on range-rate measurements (discussed in Section 2.2), any simulated data with a station elevation less than $10°$ were erased, in order to restrict the length of the ray path within the troposphere.

The covariance analysis presented in this work utilizes the information described in previous sections to estimate the accuracies on the gravity moments and tidal parameters, given different mission scenarios. The experiment is divided into 24 hr arcs centered around each closest approach (eight arcs in total for each trajectory case). The reference trajectories described in Section 2.1 were developed internally (R. Karimi, personal communication). However, in the frame of our simulations, only the initial conditions for the spacecraft state (position and velocity vectors) at the beginning of each arc were extracted from the trajectory kernels. Within each 24 hr pass, the spacecraft trajectory was propagated using MONTE and the dynamical model described in Section 3. Due to the similarity between the dynamical models and software package used for both trajectory propagation processes, we find that the reference and integrated trajectories differ by less than 10^{-1} km and 10^{-5} km s^{-1} by the end of the 24 hr integration period. These differences are negligible in the context of our analysis.

Simulated data from all arcs were combined into a multiarc solution for the solved-for vector (Parisi et al. 2021; Parisi 2023), reported in Table 2. The parameters were categorized as local (specific to each arc), global (across all arcs), and consider (whose effect on estimated coefficients is acknowledged but not estimated). The a priori uncertainties on estimated parameters were mostly left unconstrained (aside from the piecewise constant accelerations), as shown in Table 2.
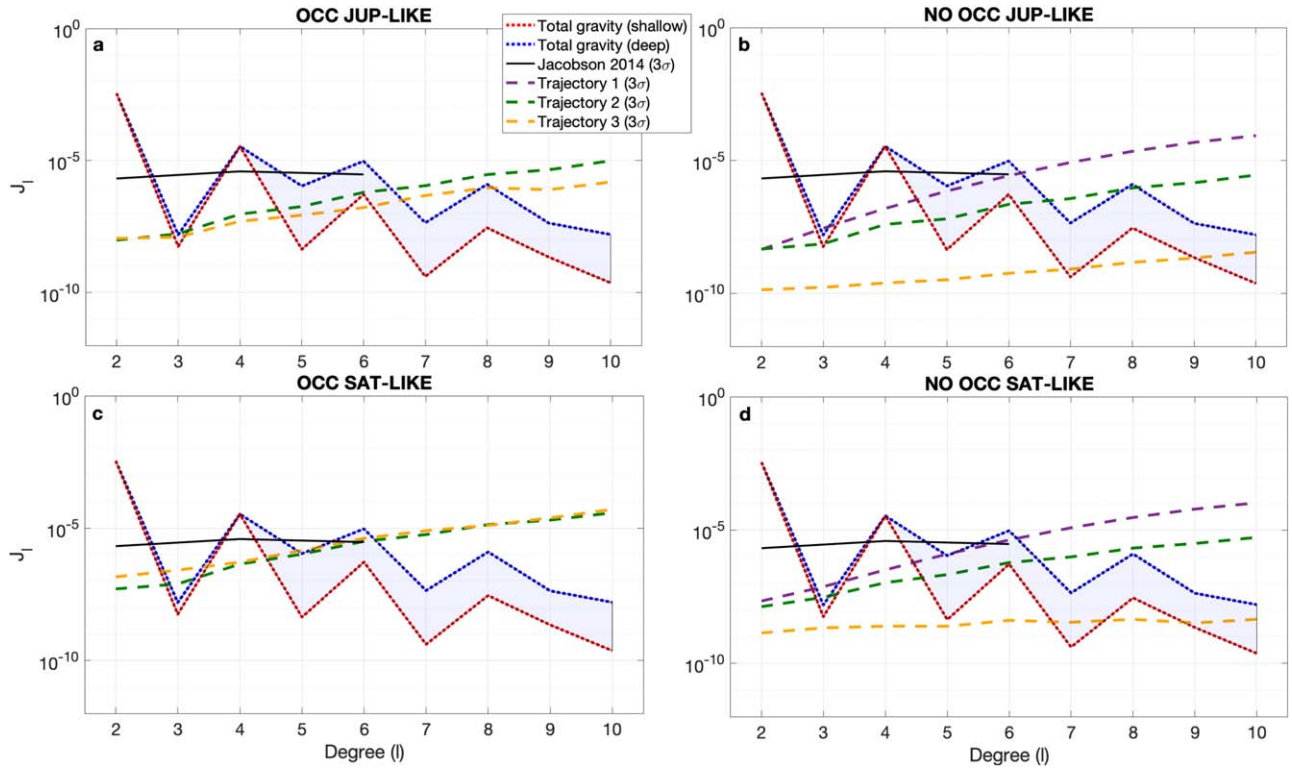
Figure 7. Estimation results for Uranus's static zonal harmonics, degree 2–10. Each panel corresponds to one of the four subcases.

5. Results

5.1. Zonal Gravity Field

Figure 7 illustrates the results of the numerical simulations in terms of attainable accuracies in the estimation of Uranus's zonal spherical harmonics, as a function of harmonic degree. They pertain to the three trajectory cases including data from the eight pericenters, and each encompasses four subcases. Among the subcases, two are associated with the anticipated noise level introduced by normal modes in the estimation of the planet's static gravity field and tidal parameters. As explained in Section 3.3, one scenario simulates the effect of normal modes by generating spacecraft accelerations similar to those observed by Juno at Jupiter (JUP-LIKE), while the other simulates accelerations approximately 20 times larger, similar to those witnessed by Cassini at Saturn (SAT-LIKE). The remaining two subcases involve the occurrence of spacecraft occultations by Uranus as observed from Earth (OCC and NO OCC), as this poses a significant challenge for gravity science. As mentioned in Section 2.1, Trajectory 1 is the only trajectory whose pericenters are visible from the ground; hence, in this instance the OCC case cannot be evaluated. Conversely, Trajectories 2 and 3 are characterized by pericenters being occulted from Earth's view by default, hindering the collection of radio science data during the time window when the spacecraft's sensitivity to the gravity field and tidal perturbation of Uranus is highest. In these instances, the OCC scenario maintains these occultation events and assesses the data loss resulting from them. Conversely, the NO OCC case simulates a precession of the spacecraft's orbital plane by 180°, making the pericenters visible from ground stations, with the caveat of spending significant resources, namely ΔV. This approach serves to quantify the impact of collecting data at close proximity to Uranus on the recovery of the planet's gravitational potential.

Trajectory 1 (purple dashed lines) stands out from other cases by showing minimal variation in results across subcases, with the uncertainty level remaining relatively constant regardless of the normal mode noise level. This consistency may stem from the spacecraft always maintaining a significant distance from the planet, even at its closest approach (with the lowest distance being ~5000 km or $1.2R_U$). Additionally, the latitudinal coverage is less than optimal, spanning only between approximately −45° and −60° latitude (Figure 1). Latitudinal coverage is extremely important for the recovery of zonal harmonics, as will be apparent in later cases. Another contributing factor may be the spacecraft's avoidance of traversing Uranus's equatorial plane between its rings and upper atmosphere, resulting in it never closely approaching the planet's equatorial region. This challenges the precise resolution of spherical harmonics, adding another element to the observed consistency in Trajectory 1's results. Compared to the spherical harmonic estimates (black solid lines) reported in Jacobson (2014a), Trajectory 1 manages to improve the 3σ uncertainties for J_2 and J_4 by approximately two and one order of magnitude, respectively, but it is unable to improve over Voyager 2 results for J_6 and beyond. Moreover, the trajectory does not allow for the detection of the smaller odd harmonics originating predominantly from the winds, thereby limiting its contribution to refining the current estimate of the depth of the winds.

The results for Trajectory 2 (green dashed lines), when Uranus occultations (OCC) are kept at pericenter, closely mirror those of Trajectory 1. This similarity is expected since, during those critical moments when the spacecraft is closest to the planet, it loses communication with Earth, adversely affecting the resolution of spherical harmonics. The results
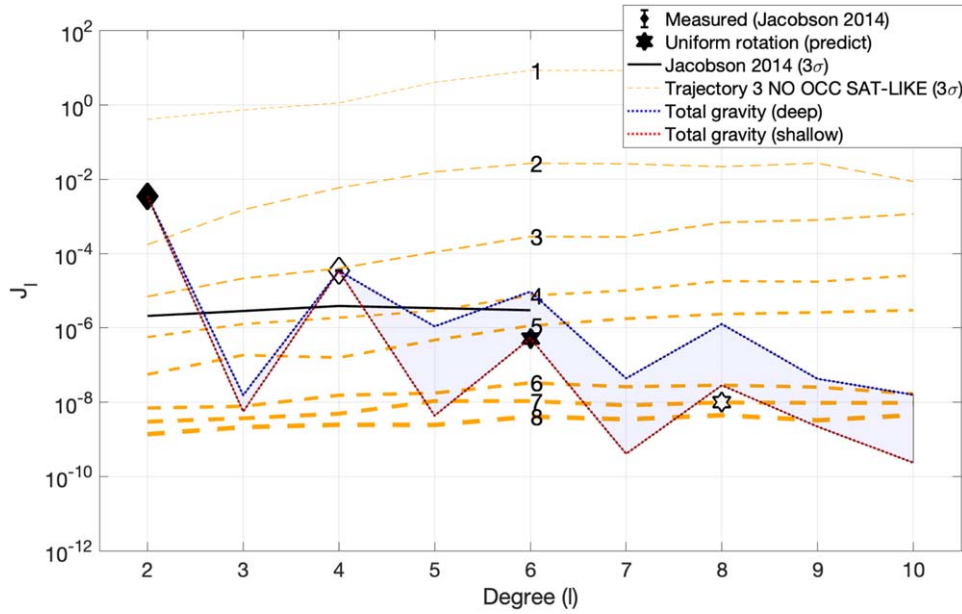
Figure 8. Estimation results for Uranus's static zonal harmonics. The uncertainty curves are specific to one of the Trajectory 3 subcases: no occultations and Saturn-like normal mode amplitudes (NO OCC SAT-LIKE).

are significantly different when the orbital plane undergoes rotation, making the pericenters visible. It is worth noting that the orbital inclination is approximately 150° for Trajectory 2, with most closest approaches occurring near the equatorial region. These conditions result in a rather favorable latitudinal coverage, spanning roughly between −30° and +15° when the altitude is below 3000 km. Under these improved conditions, there is a substantial refinement in our ability to estimate J_2 and J_4, each improving by approximately two orders of magnitude. The JUP-LIKE case even suggests a marginal detection of J_6, with an improvement of one order of magnitude compared to current estimates.

However, it is Trajectory 3 (orange dashed lines) that yields the most favorable outcome, provided that occultations are excluded for the eight pericenters. This is attributed not only to the periapses being visible from Earth but also to the fact that the spacecraft maneuver that changes the inclination significantly broadens the range of latitudinal coverage, spanning between ±30°. Moreover, the average pericenter altitude is the lowest among all three trajectory cases, approximately 1000 km. In this particular scenario, the improvements on J_2, J_4, and J_6 compared to the estimates in Jacobson (2014a) are over three orders of magnitude. Notably, only in this case does the prospect of detecting contributions to J_8 arising from uniform and differential rotation become possible, contingent on the depth of the Uranian winds. The end-of-mission uncertainties on the R.A. (α) and decl. (δ) of Uranus's pole are approximately on the order of 10^{-6} rad and 10^{-13} rad s^{-1} for the constant and linear terms, respectively. These represent roughly an order-of-magnitude improvement over the current estimates reported in Jacobson (2014a). Conversely, there is no potential for improving the determination of Uranus's rotation rate through gravity measurements only, even in the most favorable circumstances afforded by Trajectory 3, when compared to current determinations (Desch et al. 1986; Helled et al. 2010; Archinal et al. 2018).

The question arises as to whether the complete set of eight pericenters is essential to resolve the zonal spherical harmonic

coefficients J_2–J_8 with the desired accuracy (Figure 8). In order to answer this question, we considered one of the most advantageous subcases within Trajectory 3, the one that excludes Uranus occultations. However, in order to keep a conservative approach to the problem, we examined the SAT-LIKE case that features larger accelerations due to Uranus's normal modes.

The orange dashed lines, varying in thickness, represent the 3σ uncertainty curves resulting from the sequential addition of radiometric data from consecutive pericenters. A noteworthy result is that a minimum of five to six pericenters are required to improve on the existing accuracy for J_2, J_4, and J_6 by Jacobson (2014a). However, six orbits are insufficient to resolve J_8, for which we found that the complete array of eight closest approaches is necessary. If all available data are combined, we estimate a relative accuracy for J_8 between 1% and 16% at the end of the experiment, depending on the depth of the winds. For the deep wind case, the contribution from differential rotation is about two orders of magnitude larger than the contribution from uniform rotation, resulting in an overall increased detectability and lower relative uncertainty. For scientific purposes, we desire gravity components to be measured to ∼10% (e.g., Durante et al. 2020), since this level of accuracy would allow for the decoupling between the gravity field components from the interior structure and the winds. Therefore, eight pericenters are indeed required for the NO OCC SAT-LIKE case. In the OCC cases, it is not possible (among the array of trajectories we analyzed) to achieve the desired relative accuracy on J_8, regardless of the number of pericenters employed (even exceeding eight passes). The increasing number of pericenters cannot counterbalance the lack of data at close proximity and the limited geometrical coverage of the planet that it entails.

5.2. Tidal Love Number

Having confirmed the requirement for at least eight close pericenters for resolving J_8 with the desired precision, our
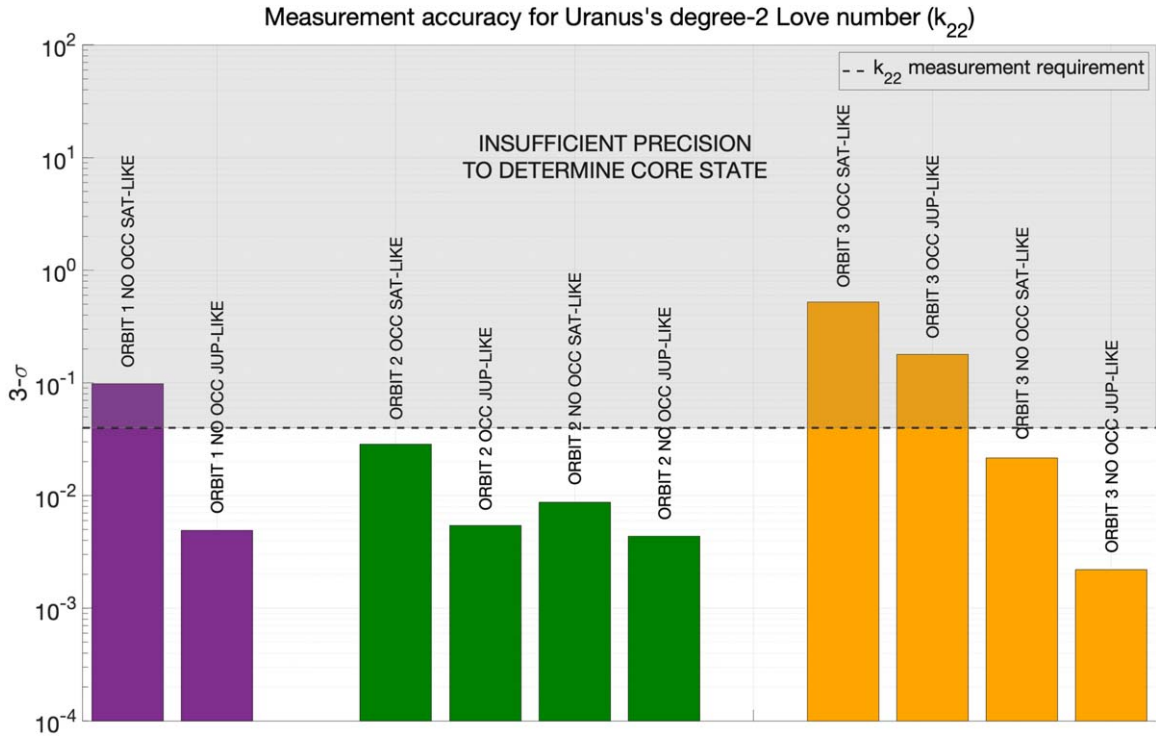
Figure 9. Estimation results for Uranus's k_{22}. Each error bar corresponds to one of the four subcases. Purple, green, and orange bars correspond to Trajectory 1, 2, and 3 subcases, respectively.

focus is shifted to the determination of the real component of the degree-2 tidal Love number, k_{22}, under the same circumstances and corresponding subcases. Figure 9 summarizes the results, presenting the 3σ uncertainty on this parameter at the end of the simulated gravity experiment. Considering that the predicted difference between the predicted values for k_{22} for a liquid versus solid core in Uranus is 0.08 (Stixrude et al. 2021), we establish half of this value (0.04) as the minimum threshold for the desired accuracy. If the 3σ uncertainty falls below this threshold, there is the potential to resolve k_{22} with adequate precision to gain insight into the planet's interior structure. Conversely, if the uncertainty is larger than this threshold (as denoted by the gray shaded area), the resolution of the tidal Love number is insufficient to discriminate the core state.

The selected trajectories strongly suggest the possibility of determining Uranus's k_{22}. Approximately 70% of subcases show a 3σ uncertainty that is at least marginally sufficient for discriminating the core state. Furthermore, in 50% of the simulations the expected end-of-mission precision is less than 0.01, indicating a robust detection of Uranus's degree-2 tidal deformations. The prevalence of positive detection is particularly evident when occultations at pericenter are either absent or disregarded (meaning that it is assumed that the orbit has been altered to bring the periapses into view from Earth). This is attributed to the spacecraft's high sensitivity to subtle changes in Uranus's gravitational potential when closest to the planet, similarly to what was found for the static gravity field determination. The impact of the effect of parameter aliasing due to the presence of normal modes is evident across all three trajectories. Uncertainties generally tend to be lower in the JUP-LIKE scenario, with the outcome especially pronounced in Trajectory 1, possibly due to its high pericenter altitudes compared to other cases.

The optimal scenario aligns with static gravity field measurements, namely Trajectory 3 when ignoring occultation and featuring Jupiter-like normal modes (NO OCC JUP-LIKE). In this case, the 3σ uncertainty can reach values as low as 0.002, well exceeding the threshold required to satisfy the science objective. This result is not surprising, as Trajectory 3 stands out for its low pericenter altitudes and favorable pericenter distributions in terms of phase angle with Ariel (Figure 6).

However, overall across subcases, Trajectory 2 is particularly favorable for measuring k_{22}, possibly due to the longitudinal coverage of each pericenter. For zonal harmonic measurement, a wider range of latitudes is advantageous, given the harmonics' axial symmetry and variability along latitude. Conversely, gravity perturbations related to the effect of the satellites' motion show the greatest variability in Uranus's equatorial plane. Hence, Trajectory 2 may perform better than Trajectory 3 with its inclination closer to equatorial. Each pericenter belonging to the former spans about 40° in longitude, whereas the second half of pericenters belonging to the latter only cover about 10° in longitude.

Finally, we address the impact of including the imaginary component of the degree-2 Love number in the vector of solved-for parameters. Because of dissipative effects due to the planet's internal friction, the tidal bulge may not align perfectly with the Uranus−Ariel direction. Instead, a small phase angle may be present, the magnitude of which is determined by the viscosity. To quantify this effect, we performed simulations where we simultaneously estimated the real and imaginary components of k_{22}. We observed that introducing this parameter may degrade the formal uncertainties reported in Figure 9 by only 12% in the most unfavorable scenario. Selecting one of the favorable scenarios would yield an end-of-

mission accuracy for both real and imaginary components of ~ 0.01.

6. Discussion and Conclusions

In this paper, we explored three mission scenarios for the UOP mission, characterized by varying pericenter altitudes, orbital inclinations, and visibility from Earth. To ensure a fair comparison, certain key features, such as the high eccentricity of the orbit and a consistent number of pericenters, were maintained across all cases. The main findings of our simulations can be summarized as follows. While all trajectories generally lead to an improvement in the Voyager 2 and ground-based estimates, the determination of Uranus's J_8 with the desired relative accuracy ($\sim 10\%$) necessitates specific conditions. For optimal results, at least eight pericenters must be visible from Earth for approximately ± 3 hr around the point of closest approach. Trajectories featuring spacecraft plunges between Uranus's rings and upper atmosphere (Trajectories 2 and 3) are preferred. Additionally, having low pericenter altitudes and near-polar inclinations contributes to favorable results across all parameters. These findings collectively favor Trajectory 3. While it is important to highlight the lack of quantification of normal modes' amplitudes, from Figures 7 and 9 we deduce that even a high level of uncertainties surrounding these parameters (SAT-LIKE scenarios) would allow for reaching the science objectives pertaining to J_8 and k_{22} by selecting Trajectory 3, provided that Uranus occultations at pericenter are avoided.

In this work, the expected achievable accuracies for the parameters of interest were estimated by conducting a covariance analysis, where we combined details about the spacecraft trajectory and instrumentation to predict the noise level and quality of the data collected in orbit. This approach involves the generation of simulated Doppler residuals, assuming a perfectly known dynamical model around the spacecraft while introducing realistic Gaussian noise on the measurements. While this technique has proved to be accurate in the past by predicting the expected formal uncertainties (see Parisi et al. 2016, 2021), we recognize a tendency for recovered formal uncertainties to be optimistic. However, the over-confidence is balanced by our conservative (if not pessimistic) approach to the inclusion of piecewise constant accelerations, especially in the Saturn-like cases. As a result, we believe that the formal uncertainties reported in this study are realistic and can be used for the purpose of mission planning.

While it is undeniable that determining the gravity moments offers a wealth of valuable information, these measurements are affected by a significant challenge: nonuniqueness. There are an infinite number of interior models, each with distinct compositions, temperature profiles, and rotational state, that can satisfactorily explain the observed external gravitational potential. This complexity underscores the difficulty in precisely resolving density and compositional gradients as presented by Movshovitz & Fortney (2022). Although the internal density profile can be accurately determined in close proximity to the 1-bar surface of the planet ($r/R_U > 0.8$), particularly beneficial for wind depth determination, uncertainties increase dramatically as we approach the planet's center (especially for $r/R_U < 0.2$). The aim of precision gravity is to narrow down the array of potential interior models to an acceptable level of uncertainty; however, even exquisite measurements of Uranus's spherical harmonics may not be sufficient to resolve among density profiles in the deep interior that have been put forward (Nettelmann et al. 2016; Helled et al. 2020; Neuenschwander & Helled 2022). On the other hand, the assessment of Uranus's degree-2 tidal component of its gravitational potential could represent a valuable tool in determining the state of Uranus's core, specifically discerning whether it is in a liquid or solid state. Our simulations indicate that an orbiter mission, given a sufficient number of low-altitude pericenters, holds the potential to accurately determine this coefficient with a level of uncertainty better than 10% (3σ), which may resolve the current ambiguity on the core state.

An additional approach to address the ambiguity of static gravity field measurements is the concept of utilizing ring and gravitational seismology to investigate the inner structures of ice giants (Friedson 2020; A'Hearn et al. 2022). These methods delve into the detection of normal modes, which are internal waves that propagate through the planet's deep interior and atmosphere and are therefore closely linked to the planet's interior structure. While two different interior models of a planet (i.e., different radial density profiles and compositions) may result in the same external gravitational potential, it is improbable that they would be characterized by identical seismic profiles. For instance, the observed resonances of Saturn's prominent rings with various internal oscillation modes (manifesting in spiral density and bending waves) have been instrumental in probing the planet's deep interior and atmosphere (Mankovich & Fuller 2021; Friedson et al. 2023). Additionally, Cassini's radio tracking data suggest the existence of pressure modes with substantially larger amplitudes (Markham et al. 2020). Similar pressure modes have been reported from ground-based spectroscopic measurements of Jupiter's surface motion (Gaulme et al. 2011; but note the conflicting results in Gulledge 2022) and Juno's radio tracking while orbiting the planet (Durante et al. 2022). These findings illustrate the potential of employing similar techniques to explore Uranus's deep interior both from the ground and with an orbiter and probe, a prospect left for future investigations.

Lastly, we discuss the potential for an extended mission beyond the eight pericenters considered in this study. Figure 8 shows that the impact of adding pericenters in the recovery of the static gravity field diminishes with the number of orbits. This limitation stands unless significant changes are made to the trajectory's characteristics, allowing access to new regions for data collection, for instance, by expanding the latitudinal range surveyed by the spacecraft at close range. However, these maneuvers come at a cost, requiring additional fuel and potentially compromising other scientific objectives. On the other hand, the Juno mission, having completed over 60 orbits around Jupiter, clearly shows the value of repeated observations of the planet's gravity field. Despite maintaining essentially the same trajectory, 7 yr of consistent data collection have proven instrumental in detecting high-degree gravity field components (Parisi et al. 2020; Kaspi et al. 2023) and tidal Love numbers (Durante et al. 2020), which may not have been possible if only eight pericenters were performed. Moreover, it has been demonstrated that longer observation periods are advantageous for estimating parameters related to the rotational state, precession rate, and moment of inertia (Le Maistre et al. 2016) of the planet. These findings strongly support the case for executing additional close approaches to the planet.

ORCID iDs

Marzia Parisi ● https://orcid.org/0000-0003-4064-6634
Mark D. Hofstadter ● https://orcid.org/0000-0002-3208-3918
Alex B. Akins ● https://orcid.org/0000-0001-8379-1909
Damon F. Landau ● https://orcid.org/0000-0002-2085-7402

References

A'Hearn, J. A., Hedman, M. M., Mankovich, C. R., et al. 2022, PSJ, 3, 194
Archinal, B. A., Acton, C. H., A'Hearn, M. F., et al. 2018, CeMDA, 130, 22
Asmar, S. W., Armstrong, J. W., Iess, L., & Tortora, P. 2005, RaSc, 40, RS2001
Asmar, S. W., Bolton, S. J., Buccino, D. R., et al. 2017, SSRv, 213, 205
Buccino, D. R., Kahan, D., Parisi, M., et al. 2021, RaSc, 56, e07387
Buccino, D. R., Oudrhiri, K., Parisi, M., et al. 2023, RaSc, 58, e2023RS007703
Cappuccio, P., Hickey, A., Durante, D., et al. 2020, P&SS, 187, 104902
Cappuccio, P., Notaro, V., di Ruscio, A., et al. 2020, ITAES, 56, 4984
Chiang, E. I., & Culter, C. J. 2003, ApJ, 599, 675
Connerney, J. E. P., Timmins, S., Oliversen, R. J., et al. 2022, JGRE, 127, e07138
de Pater, I., Gibbard, S. G., Hammel, H. B., et al. 2006, Icar, 180, 186
De Tiberis, F., Simone, L., Gelfusa, D., et al. 2011, AcAau, 68, 591
Desch, M., Connerney, J., & Kaiser, M. 1986, Natur, 322, 42
Durante, D., Parisi, M., Serra, D., et al. 2020, GeoRL, 47, e86572
Durante, D., Guillot, T., Iess, L., et al. 2022, NatCo, 13, 4632
Dutta, S., Shellabarger, E. R., Scoggins, J. B., et al. 2024, in AIAA SciTech Forum (Reston, VA: AIAA) AIAA 2024-0714
Esposito, L. W., & Colwell, J. E. 1989, Natur, 339, 605
Evans, S., Taber, W., Drain, T., et al. 2018, CEAS, 10, 79
French, R. G., Hedman, M. M., Nicholson, P. D., et al. 2024, Icar, 411, 115957
Friedson, A. J. 2020, RSPTA, 378, 20190475
Friedson, A. J., Parisi, M., Cao, Lyra, et al. 2023, Icar, 405, 115711
Fuller, J. 2014, Icar, 242, 283
Gaulme, P., Schmider, F.-X., Gay, J., Guillot, T., & Jacob, C 2011, A&A, 531, A104
Guillot, T., Miguel, Y., Militzer, B., et al. 2018, Natur, 555, 227
Gulledge, D. 2022, PhD thesis, Georgia State Univ. (doi:10.57709/32559304)
Helled, R., Anderson, J. D., & Schibert, G. 2010, Icar, 210, 446
Helled, R., Nettelmann, N., & Guillot, T. 2020, SSRv, 216, 38
Hofstadter, M., Simon, A., Atreya, S., et al. 2019, P&SS, 177, 104680

Hofstadter, M. D., Simon, A. A., Reh, K., & Elliot, J. 2017, Ice Giants Pre-Decadal Study Final Report JPL D-100520, JPL, https://www.lpi.usra.edu/NASA-academies-resources/full-report-ice-giants.pdf
Idini, B., & Stevenson, J. D. 2021, PSJ, 2, 69
Iess, L., Folkner, W. M., Durante, D., et al. 2018, Natur, 555, 220
Iess, L., Militzer, B., Kaspi, Y., et al. 2019, Sci, 364, aat2965
Jacobson, R. A. 2007, BAAS, 39, 455
Jacobson, R. A. 2014a, AJ, 148, 76
Jacobson, R. A. 2014b, Satellite Ephemeris File Release, https://naif.jpl.nasa.gov/pub/naif/generic_kernels/spk/satellites/ura111.bsp
Kaspi, Y., Showman, A. P., Hubbard, W. B., et al. 2013, Natur, 497, 344
Kaspi, Y., Galanti, E., Hubbard, W. B. , et al. 2018, Natur, 555, 223
Kaspi, Y., Galanti, E., Park, R. S., et al. 2023, NatAs, 7, 1463
Le Maistre, S., Folkner, W. M., Jacobson, J. A., et al. 2016, P&SS, 126, 78
Mankovich, C., & Fuller, J. 2021, NatAs, 5, 1103
Mankovich, C., Marley, M. S., Fortney, J., et al. 2019, ApJ, 871, 1
Mariotti, G., & Tortora, P. 2013, RaSc, 48, 111
Markham, S. , Durante, D., Iess, L., & Stevenson, D. 2020, PSJ, 1, 27
Movshovitz, N., & Fortney, J. J. 2022, PSJ, 3, 88
National Academies of Sciences, Engineering, and Medicine 2022, Origins, Worlds, and Life: A Decadal Strategy for Planetary Science and Astrobiology 2023–2032 (Washington, DC: The National Academies Press),
Nettelmann, N., Wang, K., Fortney, J. J., et al. 2016, Icar, 275, 107
Neuenschwander, B. A., & Helled, R. 2022, MNRAS, 512, 3124
Nimmo, F. 2023, PSJ, 4, 241
Notaro, V., Durante, D., & Iess, L. 2019, PSJ, 175, 34
Panning, M. P., Pike, W. T., Lognonné, P., et al. 2020, JGRE, 125, e06353
Parisi, M. 2023, PSJ, 4, 152
Parisi, M., Caruso, A., Buccino, D. R., et al. 2023, GeoRL, 50, e2023GL106637
Parisi, M., Galanti, E., Finocchiaro, S., et al. 2016, Icar, 267, 232
Parisi, M., Galanti, E., Folkner, W. M., et al. 2020, JGRE, 125, e06416
Parisi, M., Kaspi, Y., Galanti, E., et al. 2021, Sci, 374, 964
Park, R. S., Folkner, W. M., Williams, J. G., & Boggs, D. H. 2021, AJ, 161, 105
Pearl, J. C., Conrath, B. J., Hanel, R. A., et al. 1990, Icar, 84, 12
Rappaport, N., Bertotti, B., Giampieri, G., & Anderson, J. D. 1997, Icar, 126, 313
Richter, P. H. 2000, DSN Telecommunications Link Design Handbook Document 810-005, Rev E, Module 303, JPL, https://deepspace.jpl.nasa.gov/dsndocs/810-005/Binder/810-005_Binder_Change44.pdf
Rowe, J. F., Gaulme, P., Lissauer, J. J., et al. 2017, AJ, 153, 149
Simon, A., Nimmo, F., & Anderson, R. 2021, Planetary Mission Concept Study for the 2023–2032 Decadal Survey, Uranus Orbiter & Probe, NASA, https://smd-cms.nasa.gov/wp-content/uploads/2023/10/uranus-orbiter-and-probe.pdf
Soyuer, D., Neuenschwander, B., & Helled, R. 2022, AJ, 165, 27
Soyuer, D., Soubiran, F., & Helled, R. 2020, MNRAS, 498, 621
Sromovsky, L. A., de Pater, I., Fry, P. M., Hammel, H. B., & Marcus, P. 2015, Icar, 258, 192
Stixrude, L., Baroni, S., & Grasselli, F. 2021, PSJ, 2, 222
Stone, E. C. 1987, JGR, 92, 14873
Strobel, D. F., Yelle, R. V., Shemansky, D. E., & Atreya, S. K. 1991, Uranus (Tucson, AZ: Univ. Arizona Press), 65
Tanner, A. B., Border, J. S., Jongeling, A. P., et al. 2021, Embedding a Water Vapor Radiometer Within a Deep Space Network Ka-band Receiver IPN Progress Rep. 42-226, JPL, https://ipnpr.jpl.nasa.gov/progress_report/42-226/42-226F.pdf